



Cite this: DOI: 10.1039/d5cp04417k

Thermodynamic insight into AnO_2^+ bonding from ThH^+/UH^+ reactions studied by inductively coupled plasma tandem mass spectrometry

Richard M Cox, * Amanda R. Bubas and Amanda D. French

The bonding mechanisms of actinides have been a focus of fundamental research over the past few decades. In the present study, reactions of the simplest actinide-containing species, ThH^+ and UH^+ , with O_2 and CO_2 are investigated by inductively coupled plasma tandem mass spectrometry. The reactions of ThH^+ and UH^+ with O_2 are efficient, and the reactions of ThH^+ and UH^+ with CO_2 display reduced reaction efficiencies. For both reactions involving CO_2 , ThO_2^+ and UO_2^+ are observed; however, there is a clear barrier to ThO_2^+ formation whereas UO_2^+ forms through an exothermic, barrierless process. The experimental observations and available thermodynamic information are used to predict the outcomes of reactions involving the later AnH^+ . The anticipated reaction enthalpies for Pa-Am display a clear correlation with the promotion energy of An^+ to a $6d^2$ electronic configuration, $E_p(6d^2)$, although a shift in the slope of the correlation of reaction enthalpies and $E_p(6d^2)$ suggests that there is likely a change in bonding mechanism that starts with Np^+ . Similar shifts have also been noted in previous studies. Beginning with Np^+ , the $6d$ orbitals become less accessible than they are for the earlier An^+ as measured by $E_p(6d^2)$, and this accessibility of the $6d$ orbitals may drive actinide bonding.

 Received 14th November 2025,
 Accepted 12th January 2026

DOI: 10.1039/d5cp04417k

rsc.li/pccp

Introduction

The actinides (An) are commonly associated with nuclear applications, but from a fundamental perspective, An compose the bottom edge of the periodic table and display complex chemical behavior that is still not well understood. Experimental investigations of the factors that guide An reactivity and bonding remain limited. Gas-phase studies offer a direct route to examine the intrinsic chemistry of the actinides (free of perturbative solvent effects) that can provide and explain trends in bonding and reactivity across the An series.¹

The simplest actinide-containing species, An-H , has been studied using several gas-phase techniques. Surface ionization mass spectrometry was used for the isotopic analysis of U and Pu and led to the observation of UH^+ and PuH^+ ,² where the bond dissociation energy of UH^+ , $D_0(\text{U}^+-\text{H})$ was estimated to be 3.3 ± 0.5 eV. Early ion beam mass spectrometry enabled an examination of the energy dependences of the reactions of U^+ with D_2 and CD_4 leading to the formation of UD^+ .³ The bond dissociation energy of UH^+ was measured and reported as $D_0(\text{U}^+-\text{H}) = 2.9 \pm 0.2$ eV. The infrared spectra of ThH and UH in noble gas matrices have also been reported, and complementary density functional theory (DFT) calculations included

in those studies were used to characterize and assign the observed bands as well as provide mechanistic insight into product formation and reaction energetics.^{4,5}

Fourier transform ion cyclotron resonance mass spectrometry (FTICR-MS) experiments enabled the formation of UH^+ , NpH^+ , PuH^+ , AmH^+ , and CmH^+ as minor products in reactions of An^{2+} with various hydrocarbons.⁶ A subsequent study presented theoretical potential energy surfaces (PES) that mostly explained the observations noted in the FT-ICR MS experiments.⁷ Guided ion beam tandem mass spectrometry (GIBMS) was used to study the reactions of Th^+ with CH_4 and H_2O .^{8,9} ThH^+ was observed as a high energy product in both studies. Subsequent GIBMS studies of the reactions of Th^+ and U^+ with H_2 led to the determination of the BDEs of ThH^+ and UH^+ , $D_0(\text{Th}^+-\text{H})^{10} = 2.45 \pm 0.07$ eV and $D_0(\text{U}^+-\text{H})^{11} = 2.48 \pm 0.06$ eV. Experimental measurements of the electron affinities of ThH^- and UH^- accompanied by high level theoretical calculations have indicated that there is a 0.37 eV discrepancy between the theoretical and experimental $D_0(\text{Th}^+-\text{H})$ value.^{12,13} The reason for the discrepancy is unclear and remains an open investigation. Results from additional theoretical calculations for $\text{AnH}^{0/+/-}$ ($\text{An} = \text{Ac, Pa, Np, Pu}$) species have also been reported.¹²⁻¹⁵ Most recently, the BDEs of AnH^+ ($\text{An} = \text{Th-Am}$) were experimentally measured by examining the kinetic energy dependence of the reaction $\text{An}^+ + \text{CH}_4 \rightarrow \text{AnH}^+ + \text{CH}_3$.¹⁶ Table 1 summarizes the AnH^+ thermochemistry published to date.



Table 1 Experimental and theoretical bond dissociation energies (BDE) of AnH^+ (in eV)

$D_0(\text{An}^+ - \text{H})$	$E_p(6d)^a$	Experimental ^b	Theoretical ^c	Model ^d
Th	0.00	$2.96 \pm 0.81, 2.45 \pm 0.07^d$	2.82	2.45
Pa	0.10	2.94 ± 0.54	2.54	2.35
U	0.04	$2.82 \pm 0.71, 2.48 \pm 0.06^e$	2.51	2.41
		2.9 ± 0.3^f		
Np	0.00	2.87 ± 0.51	2.08	2.45
Pu	1.08	1.27 ± 0.83	0.94	1.37
Am	1.76	0.92 ± 0.74	0.69	

^a Ref. 17. ^b Unless noted otherwise ref. 16. ^c FPD calculations of AnH^+ BDEs compiled in ref. 15. See also ref. 12–14. ^d Intrinsic BDE model assuming bonding between An^+ 6d and H 1s electrons. Presented in ref. 10. ^e Ref. 11. ^f Ref. 3.

Notably, experimental measurables, like BDEs, can be a key benchmark to help validate computational methods, and these computational methods will likely prove crucial to understanding An bonding.

A key finding of the previous experimental work is that the AnH^+ BDEs are correlated to the promotion energy from the ground state to the first state that populates a 6d orbital, $E_p(6d)$,^{10,16} which mirrors earlier findings that indicate that that $D_0(\text{An}^{n+} - \text{O})$ for $n = 0–2$ are correlated to $E_p(6d^2)$.^{10,16,17} The BDEs of AnF^+ also display some correlation to $E_p(6d)$,¹⁸ which follows an earlier argument by Cox, Armentrout, and de Jong using previously reported ThF^+ , UF^+ , and PuF^+ values.¹⁰ Recent inductively coupled plasma tandem mass spectrometry (ICP-MS/MS) work has indicated that $D_0(\text{An}^+ - \text{CH}_2)$ ¹⁶ and $D_0(\text{An}^+ - \text{N})$ ¹⁹ are also correlated to $E_p(6d^2)$. The latter had previously been speculated by Armentrout and coworkers.^{20,21} While this does not rule out the involvement of 5f or 7s orbitals, the 6d orbitals are clearly important to forming actinide-ligand (AnL) bonds.

Notably, the An species described in the previous paragraph have formal oxidation states (II–IV). Theoretical studies have concluded that the 5f orbitals are more active for An in higher oxidation states.^{22–25} Classic examples include the linear OAnO^+ (V) species. Although the electrons of Th^+ do not populate the 5f orbitals in the ground state, NBO analyses have shown that 5f orbitals contribute to bonding in OThO^+ .²² Recent work has suggested that reaction kinetics may be influenced by the participation of 5f orbitals in transient species.²⁶ In that study, the comparison of the reaction kinetics between $\text{Pu}^+/\text{Nd}^+/\text{Sm}^+ + \text{NO}/\text{CO}_2$ were used to infer 5f orbital participation in the NPuO^+ intermediate with corroborating theoretical potential energy surfaces (PES). Likewise, observing the reactions starting from diatomic An species (*i.e.* AnL^+) may shed additional light on when the 5f orbitals are active in AnL bonding.

There are several reports of the reactions of AnO^+ with a variety of co-reactants.^{22,25,27–31} Generally, AnO^+ species are less reactive than their An^+ counterparts. This may be explained by the reduced availability of electrons because two An^+ valence electrons are involved in the robust AnO^+ triple bond. Alternatively, AnO^+ is likely to have increased steric restrictions

compared to An^+ and AnH^+ . AnH^+ bonding employs one of the 6d electrons of An^+ . It is of interest to study the reactions of AnH^+ to better understand the role of An^+ valence electrons and assess the impact of reduced 6d electron availability upon the observed chemistry. For the simplest polyatomic, AnH^+ , the reactions of UH^+ with background gases³² and nitriles³³ have been reported in MS^n experiments by Terhorst *et al.* However, hydrides, like UH^+ , are a known interference for analytical ICP-MS experiments.³⁴ Here we take advantage of the inductively coupled plasma's (ICP) propensity to create hydrides in the ion source to study the reactions of ThH^+ and UH^+ with O_2 and CO_2 . We also compare the observed reactions to the analogous AnO_x^{n+} ($x = 0–1, n = 1–2$) reactions to help determine the role of oxidation states in the observed chemistry. Likewise, we discuss the implications of observed thermochemical trends on An bonding.

Experimental and theoretical methods

CAUTION: the An used in this study are all radioisotopes with varying activities and half-lives. All work was done within the radiological protection controls of specialized laboratories at Pacific Northwest National Laboratory.

ICP-MS/MS

Experiments were conducted using an Agilent 8900 ICP-MS/MS located within the physical sciences facility at Pacific Northwest National Laboratory.³⁵ This instrument utilizes an ICP ion source equipped with a quartz double-pass spray chamber and $100 \mu\text{L min}^{-1}$ perfluoroalkoxy alkane (PFA) nebulizer. Hydrides are formed within the plasma source, and the resulting ions are focused through an initial quadrupole mass filter where the reactant AnH^+ are selected. The reactant ions are then focused into a collision reaction cell containing an octopole ion guide which can be pressurized with a neutral reactant gas, O_2 (Oxarc, 99.999%) or CO_2 (Oxarc, 99.999%). Residual reactant and product ions are radially confined within the octopole and drift to the exit aperture. Ions are subsequently focused through a second quadrupole mass filter to identify product ions and counted at a standard electron multiplier detector.

Stock multi-element standard solutions containing 10 ng g^{-1} of Th and U in 2% HNO_3 were prepared. Oxygen and carbon dioxide were used as reactant gases. The flow rates of O_2 and CO_2 were 0.09 and 0.18 mL min^{-1} , and 0.06 and 0.12 mL min^{-1} , respectively. Tuning parameters were optimized to provide maximum sensitivity using a 10 ng g^{-1} ^{232}Th and ^{238}U solution, with focus on increasing hydride formation. The octopole bias was adjusted in 1 V intervals from $+7 \text{ V}$ to -78 V while keeping other cell parameters constant: octopole RF peak-to-peak voltage of 180 V, axial acceleration of 0 V, and a kinetic energy discrimination (KED, the voltage difference between the octopole bias in the collision reaction cell and the second quadrupole) of -7.0 V . Data were acquired using 3 replicates, 10 sweeps/replicate and 1 s acquisition times.



Absolute reaction cross sections (σ) are calculated from the raw signal intensities using eqn (1)³⁶

$$I = I_0 e^{-\rho\sigma l} \quad (1)$$

where I is the reactant ion intensity exiting the collision cell, I_0 is the reactant ion intensity entering the collision cell, ρ is the number density of the neutral reactant in the collision cell, and l is the effective length of the collision cell. For this work I_0 is estimated as the sum of all observed ions from quadrupole 2. The physical length of the collision cell in the Agilent 8900, 10 cm, is used for l , although this is not strictly accurate because the pressure gradient will extend beyond the boundaries of the collision cell. The difference is expected to be $\leq 20\%$ and is included in the total uncertainties reported herein. Individual product ion cross sections (e.g., MO^+) are calculated as a percentage of the overall reaction cross section. Because the Agilent 8900 operates under multi-collision conditions, to compare the observed cross sections to the reaction collision limit, the cross sections observed at 1.5 and 3.0 mTorr for O_2 and 1.4 and 2.8 mTorr for CO_2 were extrapolated to zero pressure to reflect rigorous single collision conditions. Previously, we have discussed the influences on the expected number of collisions for a given neutral reactant gas and pressure.³¹ Following this analysis, the most probable number of collisions is 2–3 at the lowest energies. Although less than ideal, the two-point extrapolation was chosen to balance instrument time and operator exposure while still executing the experiment. Absolute uncertainties in the cross sections are estimated to be $\pm 50\%$ with relative uncertainties of $\pm 20\%$.

The energy in the laboratory frame is estimated from the octopole bias by eqn (2)³⁷

$$E_{\text{Lab}} = V_p + (m/m_{\text{Ar}})(5/2)k_B T_p - V_{\text{oct}} \quad (2)$$

where V_p is the plasma potential (~ 2 V), m is the mass of the M^+ reactant ion, m_{Ar} is the mass of argon (the flow gas in the ICP), k_B is Boltzmann's constant, T_p is the ion electronic temperature entering the octopole, and V_{oct} is the octopole bias. The temperature of the ion exiting the plasma is expected to be the plasma temperature, 8000–10 000 K. Previous work^{16,38,39} has indicated that T_p is between 1000–10 000 K for atomic cations. For polyatomic cations, it is less clear what the electronic distribution may be. Presumably, some excess electronic energy from the atomic cations in the source is consumed to create AnH^+ , and the electronic state density is likely less dense than the atomic electronic state density.^{10–13} Consequently, the average electronic energy available is expected to be less than that available for atomic cations. An assumption is made that there are sufficient crossings between potential energy surfaces that a pathway exists between excited state reactants and ground state products so that excess electronic energy can be treated as energy available for reaction. Theoretical calculations were previously used to examine the low-lying electronic states of ThH^+ and UH^+ .^{11,13} Based on this work, the electronic energy, E_{el} , is $E_{\text{el}}(\text{ThH}^+) = 0.37$ eV and $E_{\text{el}}(\text{UH}^+) = 0.12$ eV at 5000 K.

The energy in the center-of-mass (E_{CM}) frame represents the kinetic energy available for a chemical reaction. The relationship between E_{Lab} and E_{CM} is described by eqn (3)³⁶

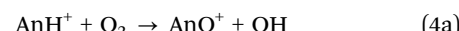
$$E_{\text{CM}} = E_{\text{Lab}} \times M/(M + m) \quad (3)$$

where M is the mass of the neutral reactant partner, O_2 (32.00 amu) or CO_2 (44.01) and m is the mass of the reactant metal hydride ion, ThH^+ (233.04 amu) or UH^+ (239.04 amu).

Experimental results



Fig. 1 displays the absolute reaction cross section of ThH^+ with O_2 as a function of kinetic energy. Fig. 2 displays the $\text{UH}^+ + \text{O}_2$ cross section. Reactions (4)–(7) were observed:



Reactions (4)–(6) are observed as barrierless exothermic processes. The reaction efficiencies (k/k_{col}) compared to the Su–Chesnavich semiclassical trajectory collision limit cross section⁴⁰ are $k/k_{\text{col}}(\text{ThH}^+) = 1.52 \pm 0.76$ and $k/k_{\text{col}}(\text{UH}^+) = 1.26 \pm 0.63$ calculated as an average from all energies < 1 eV.

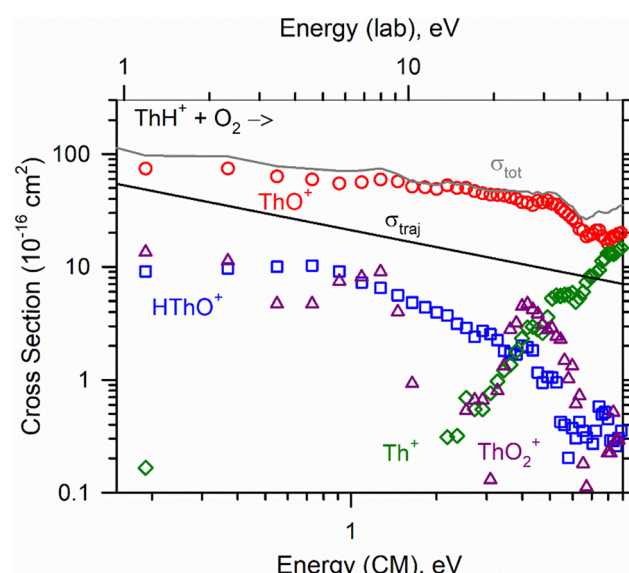


Fig. 1 The absolute reaction cross section of $\text{ThH}^+ + \text{O}_2$ as a function of kinetic energy in the laboratory frame (upper x axis) and center-of-mass frame (lower x axis). The sum of the product cross sections (σ_{tot}) is represented by a solid gray line. Individual products are ThO^+ (red circles), HThO^+ (blue squares), Th^+ (green diamonds), and ThO_2^+ (purple triangles). The Su–Chesnavich semi-classical trajectory (σ_{traj}) collision limit⁴⁰ is represented by a solid black line.



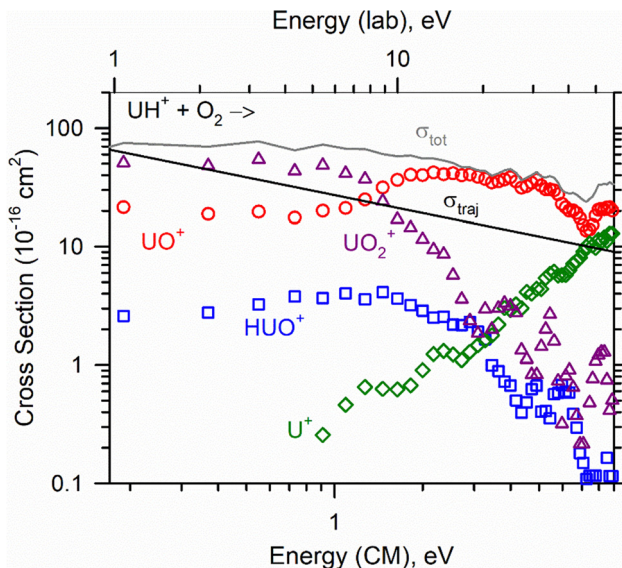


Fig. 2 The absolute reaction cross section of $\text{UH}^+ + \text{O}_2$ as a function of kinetic energy in the laboratory frame (upper x axis) and center-of-mass frame (lower x axis). The sum of the product cross sections (σ_{tot}) is represented by a solid gray line. Individual products are UO^+ (red circles), HUO^+ (blue squares), U^+ (green diamonds), and UO_2^+ (purple triangles). The Su-Chesnavich semi-classical trajectory (σ_{traj}) collision limit⁴⁰ is represented by a solid black line.

To our knowledge, k/k_{col} has not been reported for the reactions of ThH^+ and UH^+ with O_2 . Guided ion beam tandem mass spectrometry (GIBMS) experiments have reported reaction efficiencies of $k/k_{\text{col}} = 1.21 \pm 0.24$ for $\text{Th}^+ + \text{O}_2$ ⁴¹ and $k/k_{\text{col}} = 1.1 \pm 0.2$ for $\text{U}^+ + \text{O}_2$,⁴² FTICR-MS experiments by Santos *et al.*²⁷ reported $k/k_{\text{col}} = 0.86 \pm 0.43$ and $k/k_{\text{col}} = 0.68 \pm 0.34$, for the reactions of Th^+ and U^+ with O_2 , respectively. Earlier FTICR-MS studies of the same reactions from Cornehl *et al.*⁴³ reported $k/k_{\text{col}} = 1.12 \pm 0.45$ and $k/k_{\text{col}} = 1.17 \pm 0.47$ for Th^+ and U^+ , respectively. The reaction (4) (ThH^+) rate does not appear to be significantly hindered by the H-ligand compared to the atomic rate. A comparison of $\text{AnH}^+ k/k_{\text{col}}$ to that for An^+ and AnO^+ is summarized in Table 2.

The product distribution is also different between ThH^+ and UH^+ . For ThH^+ at the lowest energy, the dominant product is ThO^+ (reaction (4)). ThO_2^+ (reaction (6)) is the second most abundant product, while $[\text{Th}, \text{O}, \text{H}]^+$ (reaction (5)) is a minor product. Note that previous theoretical work^{9,45,46} indicates that $[\text{Th}, \text{O}, \text{H}]^+$ is likely HThO^+ . This structure will be adopted for future discussion of $[\text{An}, \text{O}, \text{H}]^+$. At slightly higher energies ($\sim 0.5\text{--}1.0$), HThO^+ becomes the second most abundant product. For UH^+ at the lowest energy, the dominant product is UO_2^+ (reaction (6)). UO^+ (reaction (4)) is the second most abundant product, while HUO^+ (reaction (5)) is a minor product. Product branching remains relatively consistent for energies below 1 eV. Differences in the product distributions likely result from thermodynamic drivers. For example, $D_0(\text{OU}^+ - \text{O}) = 7.56 \pm 0.12 \text{ eV}^{25} \gg D_0(\text{OTh}^+ - \text{O}) = 4.87 \pm 0.04 \text{ eV}^{22}$ so reaction (6) is significantly favored for UH^+ compared to ThH^+ . Reaction thermodynamics are discussed in greater detail below.

Table 2 A comparison of An^{n+} ($\text{An} = \text{Th}, \text{U}; n = 1, 2$) and ThL^+ and UL^+ ($\text{L} = \text{H}, \text{O}$) reaction efficiencies (k/k_{col})^a

$\text{AnL}^+ + \text{OR}$	ICP-MS/MS ^b	GIBMS ^c	FTICR-MS ^d
$\text{Th}^+ + \text{O}_2$		1.21 ± 0.24	$0.86 \pm 0.43; 1.12 \pm 0.45$
$\text{Th}^{2+} + \text{O}_2$			0.56 ± 0.28
$\text{ThH}^+ + \text{O}_2$	1.52 ± 0.76		
$\text{ThO}^+ + \text{O}_2$		NR ^e	NR ^e
$\text{U}^+ + \text{O}_2$		1.1 ± 0.2	$0.68 \pm 0.34; 1.17 \pm 0.47$
$\text{U}^{2+} + \text{O}_2$			0.53 ± 0.26
$\text{UH}^+ + \text{O}_2$	1.26 ± 0.63		
$\text{UO}^+ + \text{O}_2$		1.16 ± 0.23	$0.45 \pm 0.23; 0.95 \pm 0.38$
$\text{Th}^+ + \text{CO}_2$	1.19 ± 0.60	0.88 ± 0.18	$0.35 \pm 0.18; 0.95 \pm 0.33$
$\text{Th}^{2+} + \text{CO}_2$			0.55 ± 0.28
$\text{ThH}^+ + \text{CO}_2$	0.49 ± 0.25		
$\text{ThO}^+ + \text{CO}_2$		NR ^e	NR ^e
$\text{U}^+ + \text{CO}_2$	0.93 ± 0.47	1.18 ± 0.24	$0.29 \pm 0.15; 1.02 \pm 0.36$
$\text{U}^{2+} + \text{CO}_2$	0.72 ± 0.36		0.38 ± 0.17
$\text{UH}^+ + \text{CO}_2$	0.36 ± 0.18		
$\text{UO}^+ + \text{CO}_2$		0.02 ± 0.01^f	$0.004 \pm 0.002; 0.002 \pm 0.001$

^a Reaction efficiencies are calculated relative to the Su-Chesnavich semiclassical trajectory collision limit. See ref. 40. ^b This work for AnH^+ . Ref. 39 for An^+ . U^{2+} can be found in the SI Section. ^c Ref. 22, 25, 31, 41 and 42. ^d Ref. 27, 43 and 44. ^e NR = no observed reaction at lowest energy studied. ^f Calculated from ref. 25.

Product branching ratios are summarized in Table 3. Fig. S1–S4 also break down the branching ratios as a function of kinetic energy.

At higher energies the product An^+ is observed with apparent thresholds of 1.5 eV for Th^+ and 0.8 eV for U^+ . This likely can be attributed to reaction (7a), which is a collision induced dissociation (CID) reaction. GIBMS work indicates that the threshold for this process should be ≈ 2.5 eV for both ThH^+ and UH^+ (see Table 1).^{10,11,16} Alternatively, the hydroperoxyl radical could be formed through reaction (7b). Given $D_0(\text{O}_2 - \text{H}) = 2.24 \pm 0.01$ eV, the reaction (7b) threshold should be ≈ 0.25 eV for both ThH^+ and UH^+ . Exact assignment of the reaction is difficult because the ICP-MS/MS data is extrapolated from multicolisional conditions to “zero pressure” single collision conditions. Previous work has indicated that while this extrapolation is reasonable, the cross section may retain some multicolisional character.^{16,39} Multicolisional conditions may lead to observable artifacts such as an

Table 3 Product branching ratios at select energies ≤ 1 eV. Relative uncertainty is $\pm 10\%$

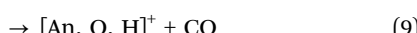
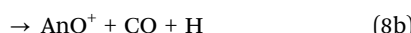
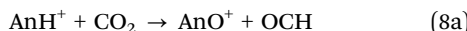
Reaction	Product	0.1 eV	0.5 eV	1 eV
$\text{ThH}^+ + \text{O}_2 \rightarrow$	ThO^+	0.70	0.81	0.79
	HThO^+	0.09	0.13	0.10
	ThO_2^+	0.21	0.06	0.11
$\text{UH}^+ + \text{O}_2 \rightarrow$	UO^+	0.31	0.26	0.32
	HUO^+	0.04	0.04	0.06
	UO_2^+	0.65	0.70	0.62
$\text{ThH}^+ + \text{CO}_2 \rightarrow$	ThO^+	0.45	0.47	0.47
	HThO^+	0.55	0.53	0.53
	ThO_2^+	0.00	0.00	0.00
$\text{UH}^+ + \text{CO}_2 \rightarrow$	UO^+	0.28	0.31	0.40
	HUO^+	0.47	0.51	0.60
	UO_2^+	0.25	0.18	0.00



apparent threshold that is shifted to lower energies relative to the thermodynamic threshold. Furthermore, AnH^+ can be partially activated upon collision storing some energy within rovibrational modes so that subsequent collisions may remove the ligand at lower energies. By contrast, competition with the more favorable reactions (4)–(6) may also delay the onset of reaction (7b). Consequently, An^+ may be formed through either mechanism; nevertheless, the observed thresholds in Fig. 1 and 2 are consistent with $D_0(\text{Th}^+ - \text{H}) = 2.45 \pm 0.07 \text{ eV}$ and $D_0(\text{U}^+ - \text{H}) = 2.48 \pm 0.06 \text{ eV}$ reported in GIBMS studies.^{10,11}

$\text{AnH}^+ + \text{CO}_2$

Fig. 3 and 4 display the absolute reaction cross section of ThH^+ and UH^+ with CO_2 as a function of kinetic energy. Reactions (8)–(11) were observed:



The observed reaction efficiencies are $k/k_{\text{col}}(\text{ThH}^+) = 0.49 \pm 0.25$ and $k/k_{\text{col}}(\text{UH}^+) = 0.36 \pm 0.18$. Like $\text{AnH}^+ + \text{O}_2$, the reaction of AnH^+ with CO_2 has not been previously reported. The reactions of $\text{An}^+ + \text{CO}_2$ have been previously reported for ICP-MS/MS, GIBMS, and FTICR-MS.^{25,27,30,31,39} Reaction efficiencies are

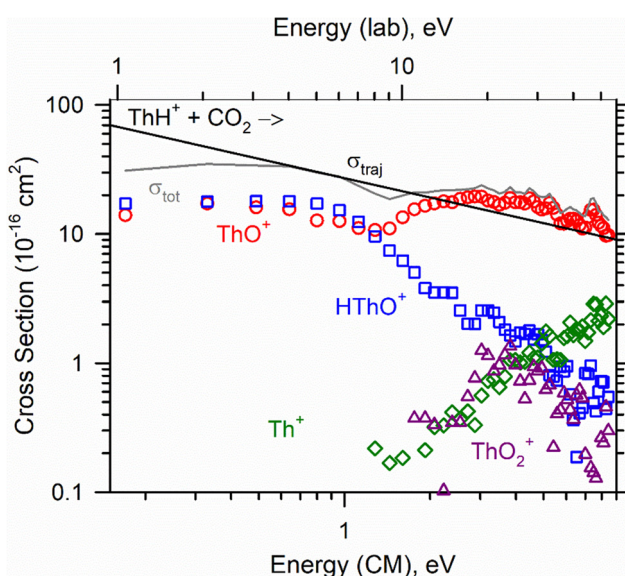


Fig. 3 The absolute reaction cross section of $\text{ThH}^+ + \text{CO}_2$ as a function of kinetic energy in the laboratory frame (upper x axis) and center-of-mass frame (lower x axis). The sum of the product cross sections (σ_{tot}) is represented by a solid gray line. Individual products are ThO^+ (red circles), HThO^+ (blue squares), Th^+ (green diamonds), and ThO_2^+ (purple triangles). The Su-Chesnavich semi-classical trajectory (σ_{traj}) collision limit⁴⁰ is represented by a solid black line.

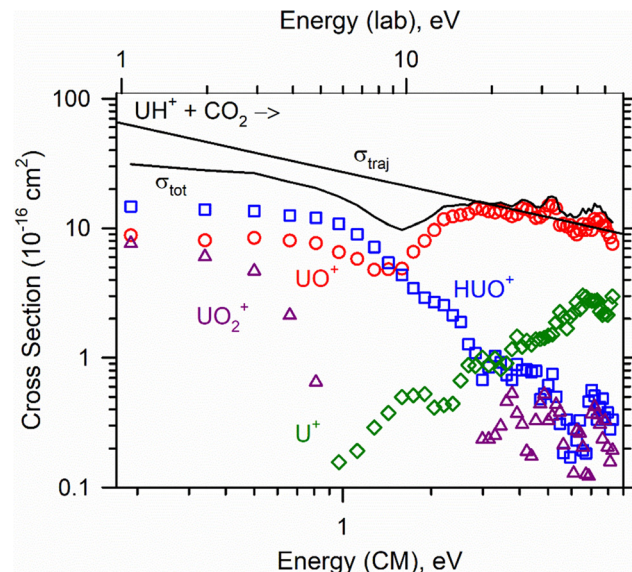


Fig. 4 The absolute reaction cross section of $\text{UH}^+ + \text{CO}_2$ as a function of kinetic energy in the laboratory frame (upper x axis) and center-of-mass frame (lower x axis). The sum of the product cross sections (σ_{tot}) is represented by a solid gray line. Individual products are UO^+ (red circles), HUO^+ (blue squares), U^+ (green diamonds), and UO_2^+ (purple triangles). The Su-Chesnavich semi-classical trajectory (σ_{traj}) collision limit⁴⁰ is represented by a solid black line.

listed in Table 2. For the atomic cations, ICP-MS/MS,³⁹ GIBMS,³¹ and FTICR-MS⁴³ reported values agree very well with the exception of the FTICR-MS efficiencies reported by Santos *et al.*²⁷ The AnH^+ reaction efficiencies are significantly reduced from the atomic reaction efficiencies. Table 2 also lists k/k_{col} for AnO^+ reported from GIBMS and FTICR-MS experiments.^{25,27,31,43,44} While $k/k_{\text{col}}(\text{AnH}^+)$ is significantly reduced from $k/k_{\text{col}}(\text{An}^+)$, $k/k_{\text{col}}(\text{AnH}^+) \gg k/k_{\text{col}}(\text{AnO}^+)$, see Table 2. For $\text{ThO}^+ + \text{CO}_2$, $D_0(\text{OTh}^+ - \text{O}) = 4.87 \pm 0.04 \text{ eV}^{22} < D_0(\text{OC} - \text{O}) = 5.45 \text{ eV}^{47}$, so no reaction is expected. However, $D_0(\text{OU}^+ - \text{O}) = 7.56 \pm 0.12 \text{ eV}^{25} \gg D_0(\text{OC} - \text{O}) = 5.45 \text{ eV}$, so thermodynamics do not explain the low reaction efficiency. Note also that by GIBMS,³¹ which measures the reaction energy dependence, the observed reaction threshold (E_0) for $\text{ThO}^+ + \text{CO}_2$ did not match the thermodynamic threshold, which indicates the presence of some barrier to reaction.

Unlike $\text{AnH}^+ + \text{O}_2$, the primary reaction observed with CO_2 was reaction (9). For ThH^+ , HThO^+ was slightly favored by $\text{HThO}^+/\text{ThO}^+ = 55/45$ for all energies $\leq 1 \text{ eV}$. For UH^+ , the branching is $\text{HUO}^+/\text{UO}^+ = 60/40$ (note UO_2^+ has been removed for two energies, see Table 3) for all energies $\leq 1 \text{ eV}$. Reaction (10) was observed for UH^+ at the lowest energies, but this product was no longer observed by 1 eV with a rapid decline occurring at $\approx 0.4 \text{ eV}$. A slight increase in the reaction (8) cross section occurs in this region, which may suggest a connection between the two channels, possibly loss of an O ligand from AnO_2^+ , but the energy resolution in Fig. 4 is not sufficient to definitively establish this argument. Reaction (10) is not observed until higher energies for ThH^+ with an apparent threshold of 2 eV. Reaction (11) is presumably a CID reaction, although the formation of HCO_2 is conceivably possible.



Apparent thresholds of 1.5 and 1 eV were observed for ThH^+ and UH^+ , respectively. Despite the possible multicollisional character retained in the reaction (11) cross sections, these observed thresholds are likely consistent with the established BDEs of ThH^+ and AnH^+ .

Discussion

Comparison of reaction rates

The reaction efficiencies of An^{n+} ($\text{An} = \text{Th, U}; n = 1, 2$) and AnL^+ ($\text{L} = \text{H, O}$) with O_2 and CO_2 from ICP-MS/MS,³⁹ GIBMS,^{22,25,31,41,42} and FTICR-MS^{27,43,44} reactions are listed in Table 2. For these reactions, the precursor ion includes An in nominal oxidation states of I–III. ICP-MS/MS data available for the reaction $\text{U}^{2+} + \text{CO}_2$ is also included in Table 2. The cross section for this reaction can be found in Fig. S5 in the SI Section.

In general, the observed ICP-MS/MS k/k_{col} for atomic cations matches reasonably well with the GIBMS measurements within experimental uncertainty. Likewise, the observed efficiencies from ICP-MS/MS are consistent with the Cornehl *et al.* FTICR-MS⁴³ results. The FTICR-MS results from Gibson and coworkers are an average factor of 3 ± 1 times lower than the GIBMS and ICP-MS/MS values, Table 3. The difference between GIBMS and FTICR-MS k/k_{col} have been noted previously.³¹ Discrepancies between the reaction efficiencies reported by ICP-MS/MS, GIBMS, and FTICR-MS can likely be attributed to differences in the starting electronic energy distributions and collision conditions achieved by each of the methods.

The FTICR-MS work from Gibson and coworkers^{27,44} are the most complete for An (I–III) starting oxidation states. For the reactions $\text{ThO}^+ + \text{O}_2/\text{CO}_2$, no reaction was observed. This result is not surprising because both reactions are endothermic as confirmed by GIBMS experiments.^{22,31} All other reactions were observed by FTICR-MS. For $\text{An}^{n+} + \text{O}_2$ ($n = 1, 2$) the reaction efficiency decreases slightly with increasing oxidation state (although with overlapping uncertainty). For $\text{UO}^+ + \text{O}_2$, the reaction efficiency also decreases slightly but is still within uncertainty of both U^{n+} ($n = 1, 2$) reactions. By contrast, the efficiency of $\text{UO}_x^+ (x = 0, 1) + \text{O}_2$ measured by GIBMS are identical within experimental uncertainty.⁴² The FTICR-MS reaction trend for An^{n+} ($n = 1, 2$) + CO_2 appears to be reversed, yet the efficiency for $\text{UO}^+ + \text{CO}_2$ is significantly reduced compared to $\text{U}^{n+} + \text{CO}_2$. This result is echoed in the GIBMS report.²⁵

At present, a complete reaction set is not available for ICP-MS/MS. Assuming that the ICP-MS/MS reaction efficiencies are similar to those reported by GIBMS, then the reaction efficiency may increase slightly for $\text{AnH}^+ + \text{O}_2$ compared to $\text{An}^+ + \text{O}_2$ but would be within the combined experimental uncertainties. A similar result may be expected for An^{2+} given the historical differences between FTICR-MS, GIBMS, and ICP-MS/MS. Reaction enthalpies calculated from AnO_x^{n+} ($n = 0–2; x = 1, 2$) values compiled by Marçalo and Gibson¹⁷ indicate that all the O_2 reactions in Table 2 will have similar thermodynamic drivers (except $\text{ThO}^+ + \text{O}_2$). Likewise, Table 4 indicates that the thermodynamics associated with AnH^+ reactions with O_2 will be similar. For the CO_2 reactions in Table 2, there is a substantial difference between $\text{An}^+ + \text{CO}_2$ and $\text{AnH}^+ + \text{CO}_2$ reaction efficiencies. Table 4 indicates ≈ 0.5 eV difference in reaction enthalpies.

The thermodynamics of the reactions observed in this work are discussed in greater detail in the next section. Table S1 also compiles the thermodynamic information for the reactions listed in Table 2. For $\text{An} \geq \text{Np}^+$, there is a significant difference in thermodynamics between oxidation states. Marçalo and Gibson tie this difference to $E_p(6d^2)$.¹⁷ Because $E_p(6d^2)$ are a rough measure of the energy of the 6d orbitals relative to the 5f orbitals populated in most An^{n+} ground states, the difference between reactivity observed in Table 2 may be a function of the accessibility of the 6d orbitals. Conversely, the difference between An reactivity with O_2 and CO_2 follow similar trends regardless of the An oxidation state. The reduced reactivity of CO_2 has been discussed in greater detail previously but has been tied to the weak interaction of a late intermediate along the potential energy surface.^{26,31,39,48}

An^+ thermochemistry

Most observed reactions are clearly exothermic reactions that seemingly will only provide upper or lower limits to BDEs. Nevertheless, the reactions here may refine existing or provide new thermodynamic values. The expected reaction enthalpies are discussed below.

The reaction enthalpy ($\Delta_r H_0^\circ$) for the ligand exchange reactions, reactions (4) and (8), are:

$$\Delta_r H_0^\circ(4) = D_0(\text{An}^+ - \text{H}) + D_0(\text{O} - \text{O}) - D_0(\text{An}^+ - \text{O}) - D_0(\text{O} - \text{H}) \quad (12)$$

Table 4 Bond dissociation energies of X–L and LX–O (X = C, O, An^+ , L = H, O) and reaction enthalpies in eV

X	$D_0(\text{X}-\text{H})^a$	$D_0(\text{X}-\text{O})^b$	$D_0(\text{OX}-\text{H})^c$	$D_0(\text{OX}-\text{O})^b$	$\Delta_r H_0^\circ(4)^d$	$\Delta_r H_0^\circ(8)^e$	$\Delta_r H_0^\circ(6)^f$	$\Delta_r H_0^\circ(10)^g$
C	3.53 ^c	11.09 ^c	1.81	5.45 ^c				
O	4.44 ^c	5.11 ^c	2.24					
Th^+	2.45 ± 0.07^h	8.57 ± 0.14^i		4.87 ± 0.04^j	-5.45 ± 0.16	-2.48 ± 0.16	-5.88 ± 0.16	2.02 ± 0.16
Pa^+	2.94 ± 0.54	8.29 ± 0.52		8.08 ± 0.30	-4.68 ± 0.75	-1.71 ± 0.75	-8.33 ± 0.81	-0.43 ± 0.81
U^+	2.48 ± 0.06^k	8.01 ± 0.13^l		7.56 ± 0.12^m	-4.87 ± 0.15	-1.90 ± 0.15	-7.99 ± 0.19	-0.09 ± 0.19
Np^+	2.87 ± 0.51	7.88 ± 0.10		6.32 ± 0.23	-4.34 ± 0.52	-1.37 ± 0.52	-6.22 ± 0.57	1.68 ± 0.57
Pu^+	1.27 ± 0.83	6.75 ± 0.20		5.28 ± 0.39	-4.81 ± 0.85	-1.84 ± 0.85	-5.64 ± 0.94	2.26 ± 0.94
Am^+	0.92 ± 0.74	5.80 ± 0.29		4.25 ± 0.58	-4.21 ± 0.79	-1.24 ± 0.79	-4.02 ± 0.98	3.88 ± 0.98

^a Ref. 16 unless indicated otherwise. ^b Ref. 17 unless indicated otherwise. ^c NIST Chemistry Webbook unless indicated otherwise. ^d See eqn (12). ^e See eqn (13). ^f See eqn (16). ^g See eqn (17). ^h Ref. 10. ⁱ Ref. 41. ^j Ref. 22. ^k Ref. 11. ^l Ref. 42. ^m Ref. 25.



$$\Delta_r H_0^\circ(8) = D_0(\text{An}^+ - \text{H}) + D_0(\text{OC} - \text{O}) - D_0(\text{An}^+ - \text{O}) - D_0(\text{OC} - \text{H}) \quad (13)$$

Existing thermochemical values are listed in Table 4. Both reaction (4) and (8) are quite exothermic. $\Delta_r H_0^\circ(4) = -5.45$ and -4.87 eV for ThH^+ and UH^+ , respectively, while $\Delta_r H_0^\circ(8) = -2.48$ and -1.90 eV. For the other An, the more discerning reaction (8) should be exothermic if $D_0(\text{An}^+ - \text{O}) \geq D_0(\text{An}^+ - \text{H}) + 3.64$ eV. From $D_0(\text{An}^+ - \text{H})$ listed in Table 4, reaction (8) should be exothermic for $\text{An}^+ = \text{Th}^+ - \text{Am}^+$.

For reactions (5) and (9), the reaction enthalpies are:

$$\Delta_r H_0^\circ(5) = D_0(\text{O} - \text{O}) - D_0(\text{HAn}^+ - \text{O}) \quad (14)$$

$$\Delta_r H_0^\circ(9) = D_0(\text{OC} - \text{O}) - D_0(\text{HAn}^+ - \text{O}) \quad (15)$$

Consequently, reactions (5) and (9) are exothermic if $D_0(\text{HAn}^+ - \text{O}) \geq D_0(\text{O} - \text{O})/D_0(\text{OC} - \text{O})$. Fig. 3 and 4 indicate that $D_0(\text{HAn}^+ - \text{O}) \geq D_0(\text{OC} - \text{O}) = 5.45$ eV for both Th^+ and U^+ . The branching ratios may provide additional information to refine $D_0(\text{HAn}^+ - \text{O})$. Assuming that the primary driver to the branching ratios is the reaction enthalpy, then ${}^\circ\Delta_r H_0^\circ(9) \leq {}^\circ\Delta_r H_0^\circ(8) = -2.48$ and -1.90 eV for ThH^+ and UH^+ . This is true for $D_0(\text{HTh}^+ - \text{O}) \geq 7.93$ and $D_0(\text{HU}^+ - \text{O}) \geq 7.38$ eV. Because reaction dynamics are controlled by more than the thermodynamic driver, the BDEs may not be this large. Nevertheless, comparison of theoretical bond distances⁹ $r(\text{Th}^+ - \text{O}) = 1.79$ Å and $r(\text{HTh}^+ - \text{O}) = 1.80$ Å indicates that both the ThO^+ and HThO^+ BDEs are likely of similar strength, consistent with $D_0(\text{HTh}^+ - \text{O}) \geq 7.93$ eV.

For reaction (6) and (10), the reaction enthalpies are:

$$\Delta_r H_0^\circ(6) = D_0(\text{An}^+ - \text{H}) + D_0(\text{O} - \text{O}) - D_0(\text{OAn}^+ - \text{O}) - D_0(\text{An}^+ - \text{O}) \quad (16)$$

$$\Delta_r H_0^\circ(10) = D_0(\text{An}^+ - \text{H}) + D_0(\text{OC} - \text{O}) + D_0(\text{C} - \text{O}) - D_0(\text{OAn}^+ - \text{O}) - D_0(\text{An}^+ - \text{O}) - D_0(\text{C} - \text{H}) \quad (17)$$

$\Delta_r H_0^\circ(10) = 2.02 \pm 0.16$ and -0.09 ± 0.19 eV for ThH^+ and UH^+ , respectively. The apparent threshold observed for reaction (10) in Fig. 3 is consistent with $\Delta_r H_0^\circ(10) = 2.02 \pm 0.16$. Likewise, the observation of a barrierless exothermic reaction for reaction (10) in Fig. 4 is also consistent with $\Delta_r H_0^\circ(10) = -0.09 \pm 0.19$ eV. Notably, eqn (17) requires that $D_0(\text{OAn}^+ - \text{O}) + D_0(\text{An}^+ - \text{O}) - D_0(\text{An}^+ - \text{H}) \geq 13.01$ eV for reaction (10) to be exothermic.

Table 4 indicates that this may only be true for PaH^+ and UH^+ , although the high uncertainty in $\Delta_r H_0^\circ(10) = -0.43 \pm 0.81$ eV may indicate otherwise for PaH^+ . Observation of the energy dependence of reaction (10) may refine some of the uncertainty in the reported Pa^+ BDEs.

There is a noticeable change in the reaction (10) thermochemistry after UH^+ , as detailed in Table 4. While it has been clearly demonstrated that the 5f orbitals contribute to bonding in linear OAnO^+ , the primary participants in bonding are the 6d orbitals. Promotion energies to a state with one unpaired 6d electron are nearly equivalent in the early series $E_p(6d) \text{Th}^+ \approx E_p(6d) \text{Pa}^+ \approx E_p(6d) \text{U}^+ \approx E_p(6d) \text{Np}^+ \ll E_p(6d)$

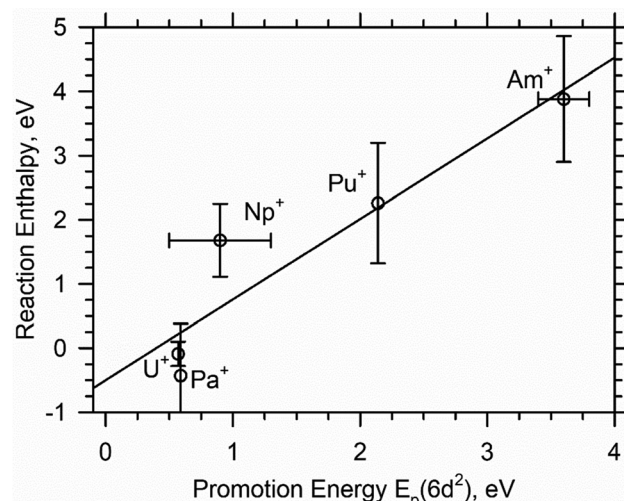


Fig. 5 The correlation between $E_p(6d^2)$ and the reaction (10) enthalpy calculated using the values found in Table 4 and eqn (17). The solid line represents the least square linear regression trend line ($-0.5 + (1.3 \pm 0.3)E_p(6d^2)$, $r^2 = 0.87$).

$\text{Pu}^+ \ll E_p(6d)$ Am^+ . For $E_p(6d)$, $E_p(6d^2)$ $\text{Th}^+ < E_p(6d^2)$ $\text{Pa}^+ \approx E_p(6d^2)$ $\text{U}^+ < E_p(6d^2)$ $\text{Np}^+ \ll E_p(6d^2)$ $\text{Pu}^+ \ll E_p(6d^2)$ Am^+ . This appears to lead to a shift in the reaction (10) enthalpy after U to a new trend as observed in Fig. 5. Note that Th^+ is excluded from this analysis because it lacks the four valence electrons to form strong dioxide bonds.

Promotion energies, $E_p(6d)$ and $E_p(6d^2)$, to some extent represent the accessibility of the 6d orbitals for bonding. Comparing these promotion energies to the $\Delta_r H_0^\circ(10)$ indicates how influential the 6d orbitals may be in forming OAnO^+ bonds. Assuming similar driving forces across the An series to OAnO^+ bonding, the trend should be linear. Fig. 5 does indicate a relatively linear correlation, yet a clear difference between the early and latter An is observed. This mirrors observations in other single ligand systems that may have deviations in observed trends between Np^+ and Pu^+ .^{16,19} This trend may suggest that there is a difference in bonding mechanism (*i.e.* orbital participation) for $\text{NpO}_2^+ - \text{AmO}_2^+$. Considering only spatial overlap as the driving force to molecular orbital formation, Fig. 5 is consistent with 5f orbital participation where the 5f orbitals are spatially larger for the early An. Armentrout and coworkers^{22,25} have demonstrated 5f orbital participation for ThO_2^+ and UO_2^+ . 5f orbital participation in hydrocarbon activation in the early An has also been argued previously to interpret FTICR-MS studies of the reactions of An^+ with hydrocarbons of varying lengths.⁴⁹ Nevertheless, 5f orbital participation in the early An cannot explain the trend observed in Fig. 5. A natural bond order analysis of AnO_2^+ ($\text{An} = \text{U-Am}$) presented by Feng, Glendening, and Peterson⁵⁰ indicates that the 5f and 6d orbital participation in both the σ and π bonding orbitals remains consistent across the four An at 50% 6d and 50% 5f (df hybrid orbital) and 50% 6d and 35% 5f (pd³f² hybrid orbital), respectively. Computational studies⁵¹ utilizing B3LYP indicate two σ and two π bonding orbitals for neutral AnO_2 . σ_g and π_g orbitals were characterized as having major



contributions from the O 2p orbitals with minor contributions from the An 6d/7s orbitals. By contrast the σ_u and π_u orbitals were characterized by major An 5f and minor O 2p orbital contributions. For the early An, the gerade orbitals are lower in energy, but this shifts between Am and Cm. The shift in the relative energy between the 5f and 6d orbitals is possibly the driving force to the shift in bonding. Between Np^+ and Pu^+ is where the 6d orbitals become less accessible. This concept can be observed in Table 1 where the $E_p(6d)$ values are listed and Table S2 where $E_p(6d^2)$ are listed. For both promotion energies, there is a clear escalation in energies from Np^+ to Pu^+ . Since the 5f/6d orbital participation does not seem to vary significantly according to theoretical observations, it is plausible that how the participation is incorporated shifts (*i.e.* orbital overlap *vs.* energy driven degeneracy).

An alternate explanation could be that NpO_2^+ is unusual. Removing the NpO_2^+ from the trend in Fig. 5 ($r^2 = 0.87$) results in an improved linear correlation (Fig. S6, $r^2 = 0.99$). This correlation excluding NpO_2^+ is stronger than both of the linear trends displayed in Fig. S7 ($r^2 = 0.95$ for both trends). NpO_2^+ may be an outlier because the electronic configuration of Np^+ is unusual for the early An series and has a $^7\text{L}_5$ ($5\text{f}^46\text{d}7\text{s}$) ground level with a low lying $^5\text{I}_4$ ($5\text{f}^47\text{s}^2$, 0.003 eV) level.⁵² Pa^+ ($n = 4$) and U^+ ($n = 5$) both have $5\text{f}^{n-2}7\text{s}^2$ ground configurations, although the $5\text{f}^{n-2}6\text{d}7\text{s}$ configurations are very low lying at 0.10 and 0.04 eV, respectively. Pu^+ ($n = 7$) and Am^+ ($n = 8$) both have $5\text{f}^{n-1}7\text{s}$ ground configurations. The 5f, 6d, and 7s orbitals of ground state Np^+ are occupied, which may suggest that they are also similar in energy. This energy similarity may drive a bonding mechanism (orbital participation) for Np^+ that is different from the other An⁺, although theoretical calculations indicate minimal differences in the bonding orbital contribution.⁵⁰ Np^+ also has a low lying $j = (5/2, 1/2)$ $5\text{f}^57\text{s}$ level at 0.01 eV, so if the ground electronic configuration is related to the observed trend in Fig. 5, then Np^+ can be grouped with both Pa^+/U^+ and Pu^+/Am^+ . The experimental uncertainty limits the conclusions that can be drawn because the trend excluding NpO_2^+ (Fig. S6) and the split trend (Fig. S7) are both reasonable. Additional experimental work is necessary to provide support for the validity of either argument.

Conclusion

The reactions of $\text{AnH}^+ + \text{O}_2/\text{CO}_2$ ($\text{An}^+ = \text{Th, U}$) may provide additional insight into An bonding. Observed reactions, in particular reaction (8), are consistent with thermochemistry derived from previous reports.^{16,17} Extending these results to the additional An in the series indicates that there may be a change in bonding mechanism that starts at Np^+ , Fig. 5. Notably, at Np^+ the 6d orbitals become less accessible than the earlier An⁺ as measured by $E_p(6d^2)$. Computational studies,⁵⁰ however, suggest that there is minimal change in the orbitals involved in AnO_2^+ bonding. Because the 5f orbitals contract with increasing atomic number, the consistent composition of the An bonding orbitals may be indicative of the

newer concept of energy driven covalency.⁵³ This concept is far from proven, but observed shifts in bonding in gas phase experiments^{16,19} are consistent with an energy driven covalency model. Although much of the focus of An chemistry has been on when and why the 5f orbitals participate in bonding, these may be the wrong questions to ask. It appears that there may be a fundamental shift in bonding mechanism between early and latter An. Additional studies should be focused on understanding that difference.

Conflicts of interest

There are no conflicts to declare.

Data availability

All data used within this document are available within this document, the accompanying supplementary information (SI), or the manuscripts referenced in this document. Supplementary information: tabulated thermochemistry values, product branching ratios as a function of kinetic energy, kinetic energy dependence absolute reaction cross section of $\text{U}^{2+} + \text{CO}_2$. See DOI: <https://doi.org/10.1039/d5cp04417k>.

Acknowledgements

The experimental data was collected with support from the Open Call Initiative under the Laboratory Directed Research and Development (LDRD) Program at Pacific Northwest National Laboratory (PNNL). Interpretation of this experimental data and writing this manuscript was supported by a U.S. Department of Energy, Office of Science, Early Career Research Program award in the Basic Energy Sciences, Division of Chemical Sciences, Geosciences, and Biosciences, Heavy Element Chemistry program under FWP 81364. PNNL is a multi-program national laboratory operated for the U.S. Department of Energy (DOE) by Battelle Memorial Institute under Contract No. DE-AC05-76RL01830.

References

- 1 M. C. Heaven and K. A. Peterson, Probing Actinide Bonds in the Gas Phase: Theory and Spectroscopy, in *Experimental and Theoretical Approaches to Actinide Chemistry*, ed. J. K. Gibson and W. A. de Jong, John Wiley & Sons Ltd, Oxford, 2018.
- 2 P. E. Moreland, D. J. Rokop and C. M. Stevens, Mass-Spectrometric Observations of Uranium and Plutonium Monohydrides Formed by Ion—Molecule Reaction, *Int. J. Mass Spectrom. Ion Phys.*, 1970, **5**(1), 127–136.
- 3 P. B. Armentrout, R. V. Hodges and J. L. Beauchamp, Endothermic Reactions of Uranium Ions with N_2 , D_2 , and CD_4 , *J. Chem. Phys.*, 1977, **66**(10), 4683.
- 4 P. F. Souter, G. P. Kushto, L. Andrews and M. Neurock, Experimental and Theoretical Evidence for the Isolation of



Thorium Hydride Molecules in Argon Matrices, *J. Phys. Chem. A*, 1997, **101**(7), 1287–1291.

5 X. Wang, L. Andrews and L. Gagliardi, Infrared Spectra of ThH_2 , ThH_4 , and the Hydride Bridging $\text{ThH}_4(\text{H}_2)_x$ ($x = 1\text{--}4$) Complexes in Solid Neon and Hydrogen, *J. Phys. Chem. A*, 2008, **112**(8), 1754–1761.

6 J. Marcalo, M. Santos and J. K. Gibson, Gas-phase Reactions of Doubly Charged Actinide Cations with Alkanes and Alkenes-Probing the Chemical Activity of 5f Electrons from Th to Cm, *Phys. Chem. Chem. Phys.*, 2011, **13**(41), 18322–18329.

7 E. Di Santo, M. Santos, M. C. Michelini, J. Marcalo, N. Russo and J. K. Gibson, Gas-Phase Reactions of the Bare Th^{2+} and U^{2+} Ions with Small Alkanes, CH_4 , C_2H_6 , and C_3H_8 : Experimental and Theoretical Study of Elementary Organoactinide Chemistry, *J. Am. Chem. Soc.*, 2011, **133**(6), 1955–1970.

8 R. M. Cox, P. B. Armentrout and W. A. de Jong, Activation of CH_4 by Th^+ as Studied by Guided Ion Beam Mass Spectrometry and Quantum Chemistry, *Inorg. Chem.*, 2015, **54**(7), 3584–3599.

9 R. M. Cox and P. B. Armentrout, Activation of Water by Thorium Cation: A Guided Ion Beam and Quantum Chemical Study, *J. Am. Soc. Mass Spectrom.*, 2019, **30**(10), 1835–1849.

10 R. M. Cox, P. B. Armentrout and W. A. de Jong, Reactions of $\text{Th}^+ + \text{H}_2$, D_2 , and HD Studied by Guided Ion Beam Tandem Mass Spectrometry and Quantum Chemical Calculations, *J. Phys. Chem. B*, 2016, **120**, 1601–1614.

11 W.-J. Zhang, M. Demireva, J. Kim, W. A. de Jong and P. B. Armentrout, Reactions of U^+ with H_2 , D_2 , and HD Studied by Guided Ion Beam Tandem Mass Spectrometry and Theory, *J. Phys. Chem. A*, 2021, **125**(36), 7825–7839.

12 G. F. de Melo, M. Vasiliu, M. Marshall, Z. Zhu, B. A. Tufekci, S. M. Ciborowski, M. Blankenhorn, R. M. Harris, K. H. Bowen and D. A. Dixon, Experimental and Computational Description of the Interaction of H and H^- with U, *J. Phys. Chem. A*, 2022, **126**(27), 4432–4443.

13 M. Vasiliu, K. A. Peterson, M. Marshall, Z. Zhu, B. A. Tufekci, K. H. Bowen and D. A. Dixon, Interaction of Th with $\text{H}^{0/-/+}$: Combined Experimental and Theoretical Thermodynamic Properties, *J. Phys. Chem. A*, 2022, **126**(2), 198–210.

14 G. F. de Melo and D. A. Dixon, Protactinium and Actinium Monohydrides: A Theoretical Study on Their Spectroscopic and Thermodynamic Properties, *J. Phys. Chem. A*, 2022, **126**(36), 6171–6184.

15 G. F. de Melo and D. A. Dixon, Energetic and Electronic Properties of $\text{NpH}^{0/-/+}$ and $\text{PuH}^{0/-/+}$, *J. Phys. Chem. A*, 2023, **127**(14), 3179–3189.

16 A. R. F. Bubas, D. Amanda, K. M. Melby, M. J. Rodriguez and R. M. Cox, The Balance of Orbital Overlap and Orbital Energy in the Activation of Methane by Actinide Cations: Insights from Inductively Coupled Plasma Tandem Mass Spectrometry, *Inorg. Chem. Front.*, 2025, **12**, 1503–1516.

17 J. Marcalo and J. K. Gibson, Gas-Phase Energetics of Actinide Oxides: An Assessment of Neutral and Cationic Monoxides and Dioxides from Thorium to Curium, *J. Phys. Chem. A*, 2009, **113**(45), 12599–12606.

18 J. K. Gibson, Bond Dissociation Energies Reveal the Participation of d Electrons in f-Element Halide Bonding, *J. Phys. Chem. A*, 2022, **126**(2), 272–285.

19 R. M. Cox, A. R. Bubas, K. M. Melby, A. D. French, M. J. Rodriguez, M. P. Prange, N. Govind, K. A. Peterson and P. B. Armentrout, The Reactions of An^+ ($\text{An}^+ = \text{Th}^+$, U^+ – Am^+) + NO Reactions Observed by Inductively Coupled Plasma Tandem Mass Spectrometry, 2025, in progress.

20 R. M. Cox, A. Kafle, P. B. Armentrout and K. A. Peterson, Bond Energy of ThN^+ : A Guided Ion Beam and Quantum Chemical Investigation of the Reactions of Thorium Cation with N_2 and NO, *J. Chem. Phys.*, 2019, **151**(3), 034304.

21 A. R. Bubas, A. Kafle, B. C. Stevenson and P. B. Armentrout, The Bond Energy of UN^+ : Guided Ion Beam Studies of the Reactions of U^+ with N_2 and NO, *J. Chem. Phys.*, 2024, **160**, 164305.

22 P. B. Armentrout and K. A. Peterson, Guided Ion Beam and Quantum Chemical Investigation of the Thermochemistry of Thorium Dioxide Cations: Thermodynamic Evidence for Participation of f Orbitals in Bonding, *Inorg. Chem.*, 2020, **59**(5), 3118–3131.

23 K. S. Otte, J. E. Niklas, C. M. Studwick, C. L. Montgomery, A. R. C. Bredar, I. A. Popov and H. S. La Pierre, Proton-Coupled Electron Transfer at the $\text{Pu}^{5+/4+}$ Couple, *J. Am. Chem. Soc.*, 2024, **146**, 21859–21867.

24 J. E. Niklas, K. S. Otte, C. M. Studwick, S. Roy Chowdhury, B. Vlaisavljevich, J. Bacsa, F. Kleemiss, I. A. Popov, H. S. La Pierre and A. Tetrahedral, Neptunium(v) Complex, *Nat. Chem.*, 2024, **16**(9), 1490–1495.

25 A. R. Bubas, W.-J. Zhang, P. B. Armentrout and A. Guided Ion Beam Investigation, of UO_2^+ Thermodynamics and f orbital Participation: Reactions of $\text{U}^+ + \text{CO}_2$, $\text{UO}^+ + \text{O}_2$, and $\text{UO}^+ + \text{CO}$, *J. Chem. Phys.*, 2023, **159**(24), 244305.

26 R. M. Cox, A. R. Bubas, K. M. Melby, A. D. French, M. J. Rodriguez, M. P. Prange and N. Govind, The Curious Case of Pu^+ : Insight on 5f Orbital Activity from Inductively Coupled Plasma Tandem Mass Spectrometry (ICP-MS/MS) Reactions, *Inorg. Chem.*, 2024, **63**(43), 20617–20624.

27 M. Santos, J. Marcalo, A. P. D. Matos, J. K. Gibson and R. G. Haire, Gas-Phase Oxidation Reactions of Neptunium and Plutonium Ions Investigated via Fourier Transform Ion Cyclotron Resonance Mass Spectrometry, *J. Phys. Chem. A*, 2002, **106**, 7190–7194.

28 M. Santos, A. P. d Matos, J. Marcalo, J. K. Gibson, R. G. Haire, R. Tyagi and R. M. Pitzer, Oxidation of Gas-Phase Protactinium Ions, Pa^+ and Pa^{2+} : Formation and Properties of $\text{PaO}_2^{2+}(\text{g})$, Protactinyl, *J. Phys. Chem. A*, 2006, **110**, 5751–5759.

29 M. Santos, J. Marcalo, J. P. Leal, A. P. D. Matos, J. K. Gibson and R. G. Haire, FTICR-MS Study of the Gas-phase Thermochemistry of Americium Oxides, *Int. J. Mass Spectrom.*, 2003, **228**, 457–465.

30 P. B. Armentrout and J. L. Beauchamp, Reactions of U^+ and UO^+ with O_2 , CO , CO_2 , COS , CS_2 and D_2O , *Chem. Phys.*, 1980, **50**, 27–36.



31 R. M. Cox, K. Harouaka, M. Citir and P. B. Armentrout, Activation of CO_2 by Actinide Cations (Th^+ , U^+ , Pu^+ , and Am^+) as Studied by Guided Ion Beam and Triple Quadrupole Mass Spectrometry, *Inorg. Chem.*, 2022, 8168–8181.

32 J. G. Terhorst, T. A. Corcovilos and M. J. van Stipdonk, Conversion of a UO_2^{2+} Precursor to UH^+ and U^+ Using Tandem Mass Spectrometry to Remove Both “yl” Oxo Ligands, *J. Am. Soc. Mass Spectrom.*, 2023, 34(11), 2439–2442.

33 J. G. Terhorst, T. A. Corcovilos, S. J. Lenze and M. J. van Stipdonk, Synthesis of Organo-Uranium(II) Species in the Gas-Phase using Reactions Between $[\text{UH}]^+$ and Nitriles, *Dalton Trans.*, 2025, 54(1), 231–238.

34 K. P. Hobbs, A. D. French, K. M. Melby, E. J. Bylaska, K. Harouaka, R. M. Cox, I. J. Arnquist and C. L. Beck, Assessing Gas-Phase Ion Reactivity of 50 Elements with NO and the Direct Application for ^{239}Pu in Complex Matrices Using ICP-MS/MS, *Anal. Chem.*, 2024, 96(15), 5807–5814.

35 K. Harouaka, C. Allen, E. Bylaska, R. M. Cox, G. C. Eiden, M. L. D. Vacri, E. W. Hoppe and I. J. Arnquist, Gas-Phase Ion-Molecule Interactions in a Collision Reaction Cell with Triple Quadrupole-Inductively Coupled Plasma Mass Spectrometry: Investigations with N_2O as the Reaction Gas, *Spectrochim. Acta, Part B*, 2021, 186, 106309.

36 P. B. Armentrout, Mass Spectrometry – Not Just a Structural Tool: The Use of Guided Ion Beam Tandem Mass Spectrometry to Determine Thermochemistry, *J. Am. Soc. Mass Spectrom.*, 2002, 13(5), 419–434.

37 N. Yamada, Kinetic Energy Discrimination in Collision/Reaction Cell ICP-MS: Theoretical Review of Principles and Limitations, *Spectrochim. Acta, Part B*, 2015, 110, 31–44.

38 A. R. Bubas, R. M. Cox, K. M. Melby, A. D. French, M. J. Rodriguez, M. P. Prange, N. Govind and P. B. Armentrout, The Reactions of Ln^+ ($\text{Ln}^+ = \text{Ce}^+$, Pr^+ , Nd^+ , Sm^+ , Eu^+) + NO Reactions Observed by Inductively Coupled Plasma Tandem Mass Spectrometry, *J. Chem. Phys.*, 2025, submitted.

39 R. M. Cox, K. M. Melby, A. D. French and M. J. Rodriguez, f-Block Reactions of Metal Cations with Carbon Dioxide Studied by Inductively Coupled Plasma Tandem Mass Spectrometry, *Phys. Chem. Chem. Phys.*, 2024, 26(1), 209–218.

40 T. Su and M. T. Bowers, Ion-Polar Molecule Collisions: The Effect of Ion Size on Ion-Polar Molecule Rate Constants: The Parameterization of the Average Dipole Orientation Theory, *Int. J. Mass Spectrom. Ion Phys.*, 1973, 12, 347–356.

41 R. M. Cox, M. Citir, P. B. Armentrout, S. R. Battey and K. A. Peterson, Bond Energies of ThO^+ and ThC^+ : A Guided Ion Beam and Quantum Chemical Investigation of the Reactions of Thorium Cation with O_2 and CO, *J. Chem. Phys.*, 2016, 144, 184309.

42 W. Zhang, A. R. E. Hunt, M. Demireva, J. Kim, K. A. Peterson and P. B. Armentrout, Bond Energies of UO^+ and UC^+ : Guided Ion Beam and Quantum Chemical Studies of the Reactions of Uranium Cation with O_2 and CO, *Isr. J. Chem.*, 2023, e202300026.

43 H. H. Cornehl, R. Wesendrup, M. Diefenbach and H. Schwarz, A Comparative Study of Oxo-Ligand Effects in the Gas-Phase Chemistry of Atomic Lanthanide and Actinide Cations, *Chem. – Eur. J.*, 1997, 3(7), 1083–1090.

44 J. K. Gibson, R. G. Haire, M. Santos, J. Marcalo and A. Pires de Matos, Oxidation Studies of Dipositive Actinide Ions, An^{2+} ($\text{An} = \text{Th, U, Np, Pu, Am}$) in the Gas Phase: Synthesis and Characterization of the Isolated Uranyl, Neptunyl, and Plutonyl Ions $\text{UO}_2^{2+}(g)$, $\text{NpO}_2^{2+}(g)$, and $\text{PuO}_2^{2+}(g)$, *J. Phys. Chem. A*, 2005, 109(12), 2768–2781.

45 G. Mazzone, M. d C. Michelini, N. Russo and E. Sicilia, Mechanistic Aspects of the Reaction of Th^+ and Th^{2+} with Water in the Gas Phase, *Inorg. Chem.*, 2008, 47(6), 2083–2088.

46 J. Zhou and H. B. Schlegel, Ab Initio Molecular Dynamics Study of the Reaction between Th^+ and H_2O , *J. Phys. Chem. A*, 2010, 114(33), 8613–8617.

47 R. D. Johnson III, NIST Computational Chemistry Comparison and Benchmark Database. <https://cccbdb.nist.gov/> (accessed April 12, 2018).

48 P. B. Armentrout and R. M. Cox, Potential Energy Surface for Reaction of $\text{Sm}^+ + \text{CO}_2 \rightarrow \text{SmO}^+ + \text{CO}$: Guided Ion Beam and Theoretical Studies, *Phys. Chem. Chem. Phys.*, 2017, 19, 11075–11088.

49 J. K. Gibson, R. G. Haire, J. Marcalo, M. Santos, A. Pires de Matos, M. K. Mrozik, R. M. Pitzer and B. E. Bursten, Gas-Phase Reactions of Hydrocarbons with An^+ and AnO^+ ($\text{An} = \text{Th, Pa, U, Np, Pu, Am, Cm}$): The Active Role of 5f Electrons in Organoprotactinium Chemistry, *Organometallics*, 2007, 26(16), 3947–3956.

50 R. Feng, E. D. Glendening and K. A. Peterson, Actinyl Cation-Cation Interactions in the Gas Phase: An Accurate Thermochemical Study, *Phys. Chem. Chem. Phys.*, 2019, 21(15), 7953–7964.

51 A. Kovacs, P. Pogany and R. J. M. Konings, Theoretical Study of Bond Distances and Dissociation Energies of Actinide Oxides AnO and AnO_2 , *Inorg. Chem.*, 2012, 51(8), 4841–4849.

52 J. E. Sansonetti and W. C. Martin, NIST Standard Reference Database 108. <https://www.nist.gov/pml/handbook-basic-atomic-spectroscopic-data>.

53 J. Su, E. R. Batista, K. S. Boland, S. E. Bone, J. A. Bradley, S. K. Cary, D. L. Clark, S. D. Conradson, A. S. Ditter, N. Kaltsosyanis, J. M. Keith, A. Kerridge, S. A. Kozimor, M. W. Löble, R. L. Martin, S. G. Minasian, V. Mocko, H. S. La Pierre, G. T. Seidler, D. K. Shuh, M. P. Wilkerson, L. E. Wolfsberg and P. Yang, Energy-Degeneracy-Driven Covalency in Actinide Bonding, *J. Am. Chem. Soc.*, 2018, 140(51), 17977–17984.

